



Article

Excitation Density Effects in the Luminescence Yield and Kinetics of MAPbBr₃ Single Crystals

Andrey N. Belsky¹, Nikita A. Fedorov¹ , Ivan A. Frolov², Irina A. Kamenskikh², Patrick Martin¹, Elizaveta D. Rubtsova², Igor N. Shpinkov^{2,3}, Dmitry A. Spassky^{3,4}, Andrey N. Vasil'ev^{3,*} , and Boris I. Zadneprovsky⁵

¹ Centre Lasers Intenses et Applications (CELIA), CNRS-CEA-University of Bordeaux, 33405 Talence, France; nikita.a.fedorov@gmail.com (N.A.F.)

² Faculty of Physics, Lomonosov Moscow State University, 119991 Moscow, Russia; ikamenskikh@bk.ru (I.A.K.); rubtsova-liza98@yandex.ru (E.D.R.); igor.shpinkov@gmail.com (I.N.S.)

³ Institute of Nuclear Physics, Lomonosov Moscow State University, 119991 Moscow, Russia; spas@srd.sinp.msu.ru or dmitry.spasskiy@ut.ee

⁴ Institute of Physics, University of Tartu, W. Ostwald Str. 1, 50411 Tartu, Estonia

⁵ All-Russian Research Institute for Synthesis of Materials, 601650 Alexandrov, Russia

* Correspondence: anv@sinp.msu.ru

Abstract: The luminescent Z-scan technique with time resolution is applied to the study of the luminescence properties of CH₃NH₃PbBr₃ single crystals representative of the family of hybrid organic–inorganic lead perovskites successfully applied recently in photovoltaics and currently investigated as potential nanosecond scintillators. The third harmonic of Ti-sapphire laser ($\lambda = 266$ nm) with a pulse duration of 26 fs and 1 kHz frequency was applied for the luminescence excitation creating the charge carriers with the estimated density from 10^{17} to 10^{21} cm⁻³ in the temperature range from 13 to 300 K. Temperature and excitation density dependence of the luminescence yield and kinetics is interpreted with the consideration of the temperature-dependent binding of electrons and holes into excitons, a saturation of defects responsible for the non-radiative relaxation channel competing with exciton creation; absorption saturation resulting in the increased penetration depth of the excitation radiation and hence the increased contribution of the re-absorption.

Keywords: hybrid organic–inorganic lead perovskites; scintillators; luminescence kinetics



Citation: Belsky, A.N.; Fedorov, N.A.; Frolov, I.A.; Kamenskikh, I.A.; Martin, P.; Rubtsova, E.D.; Shpinkov, I.N.; Spassky, D.A.; Vasil'ev, A.N.; Zadneprovsky, B.I. Excitation Density Effects in the Luminescence Yield and Kinetics of MAPbBr₃ Single Crystals. *Crystals* **2023**, *13*, 1142. <https://doi.org/10.3390/cryst13071142>

Academic Editor: Maria Gazda

Received: 15 June 2023

Revised: 12 July 2023

Accepted: 18 July 2023

Published: 22 July 2023



Copyright: © 2023 by the authors. Licensee MDPI, Basel, Switzerland. This article is an open access article distributed under the terms and conditions of the Creative Commons Attribution (CC BY) license (<https://creativecommons.org/licenses/by/4.0/>).

1. Introduction

In crystals used as scintillating materials, ionizing radiation creates regions of extremely high densities of electronic excitations. These are the regions in the vicinity of the axis of tracks created by heavy ionizing particles (protons, alpha-particles et al.), and at the end of electron tracks, energy deposition there approaches 50 to 100 eV per nanometer of particle trajectory [1–5]. The concentration of excitations created within femtosecond time in these regions reaches 10^{20} – 10^{21} elementary excitations (excitons and electron–hole pairs) per cubic centimeter. Such concentrations of excitations result in efficient interaction between them up to e-h plasma effects. Relaxation of electronic excitations and their Auger-type annihilation leads to a fast decrease in their concentration down to the values when the interaction becomes weak. If we deal with fast nanosecond and subnanosecond scintillators [6,7] their radiative relaxation is to a large extent defined by the initial relaxation phase when the concentration of the charge carriers is high. A high concentration of interacting excitations created simultaneously can be achieved by excitation of the matter by femtosecond radiation of high intensity if its photon energy falls into the range of exciton or electron–hole pair creation. The method of Z-scan designed for the measurements of non-linear absorption coefficients in the transparency region, when applied in the fundamental absorption range, allows for the investigation of luminescence yield and kinetics

as a function of controlled excitation density. Femtosecond laser radiation focused by a lens creates a substantially non-uniform distribution of electronic excitations both across the spot at the sample surface and along the depth profile [8,9]. Thus the method yields emission parameters averaged over the concentration of excitations in the laser spot. The application of this technique for the investigation of scintillating single crystals demonstrates that non-proportionality of the scintillation yield (yield dependence on the ionizing particle energy) is caused by the interaction of excitations in the regions of their high concentration, which affects scintillation kinetics as well. It was demonstrated that in some crystals (e.g., crystals with oxy-anions), high excitation density results in luminescence quenching accompanied by the acceleration of its kinetics [10–12]; in the other ones, the luminescence yield can substantially increase with the excitation intensity. For the latter case, a strong non-proportionality of the scintillation yield is observed: the yield is lower both for low energies of the ionizing particles (e.g., electrons with the energy below 10–50 KeV) and for high energies (above 200 KeV) as compared to the region of intermediate energy. Examples of such materials are ZnO, undoped CsI, and CsPbCl₃ [13]. These crystals have a low luminescence yield when excited in the fundamental absorption region (below the threshold of photon multiplication); however, their scintillation yield is reasonable when excited by X-rays or ionizing particles. Here, we present the results for one of the similar crystals, namely lead halide perovskite with an organic cation, which, together with high photoconductivity, demonstrates a good yield of subnanosecond luminescence excited by ionizing radiation. Traditional scintillators are not renowned for high photoconductivity, while crystals producing electric current in response to ionizing radiation normally do not have a substantial luminescence yield. The combination of contradictory parameters in the material under investigation is undoubtedly attractive for the study of the physics of processes under high-density excitation as well as for the practical task of the creation of scintillators with time resolution at the level of tens of picoseconds.

2. Materials and Methods

Single crystals of CH₃NH₃PbBr₃ (MAPbBr₃) with perovskite structure were synthesized using well-known anti-solvent vapor-assisted crystallization [14] but with accurate controlled diffusion of anti-solvent vapor into process solvent. The single-crystal growth was passed according to the chemical reaction:



N,N-dimethylformamide C₃H₇NO (DMF) was chosen as a solvent as it is characterized by the high solubility of MABr and PbBr₂ in it. Dichloromethane CH₂Cl₂ (DCM) was used as an anti-solvent. The crystals were grown by spontaneous crystallization method over a period of 4–5 days with low growth rates.

The resulting MAPbBr₃ single crystals are shown in Figure 1a. The crystals had a flat-cubic shape with dimensions of 8 × 8 × 3 mm³, orange color, mirror-smooth crystal faces with indexes [100], and did not contain internal inclusions. The XRD patterns of crystals (Figure 1b) contain only peaks that belong to a high-temperature cubic phase of MAPbBr₃ with *Pm* $\bar{3}$ *m* spatial group. The value of the lattice parameter was calculated as 5.913 (7) Å, which corresponds well to known estimates. The high sharpness of the XRD peaks and the absence of extraneous one indicates the high crystallinity and phase purity of the grown crystals.

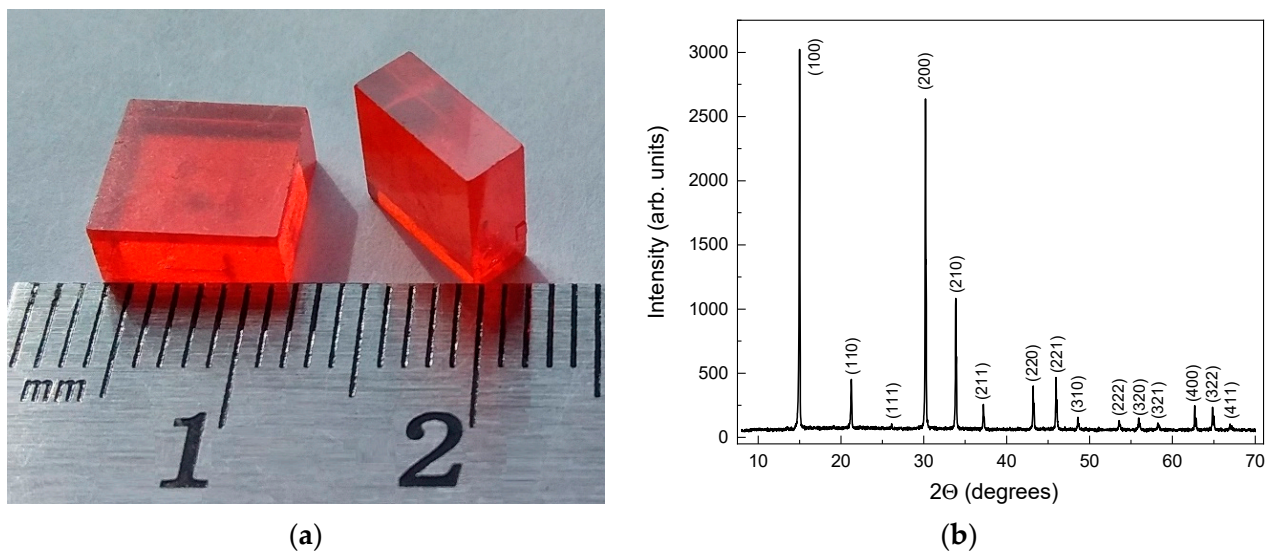


Figure 1. (a) Photo and (b) powder XRD pattern of MAPbBr₃ crystal.

The characterization of the crystal structure of MAPbBr₃ crystals was carried out by the X-ray powder diffraction method on a Rigaku Ultima IV diffractometer with Bragg–Brentano geometry, using CuK α radiation.

Luminescence emission and excitation spectra were measured using a 150 W xenon lamp (Oriental Instruments, Stratford, CT, USA), MDR-206 primary monochromator (Lomo, Saint-Petersburg, Russia), and LOT-Oriel MS-257 spectrograph (Oriental Instruments, Stratford, CT, USA) equipped with Marconi CCD detector (Marconi Applied Technologies Limited, Chelmsford, UK). Samples were mounted into Cryotrade LN-120 vacuum optical cryostat (Cryotrade Engineering, Moscow, Russia).

Luminescence emission spectra and kinetics under X-ray excitation ($h\nu = 19$ keV) were measured at the P23 station of the PETRA III storage ring at DESY (Hamburg, Germany). The experimental setup included a nitrogen cryostat, monochromator Andor Kymera 328i, equipped with an Andor iCCD detector and MCP-PMT Hamamatsu R3809U-50.

The effect of excitation density was studied using the Z-scan technique in the CELIA laboratory (Bordeaux, France). The 3rd harmonic ($\lambda = 266$ nm) of Ti:Al₂O₃ laser with pulses of 26 fs and 9 mJ/pulse at 1 kHz frequency was used for luminescence excitation [15]. The samples were in a vacuum helium cryostat with a temperature range of 13 to 300 K. The laser beam was focused onto the sample surface using a lens fixed on a platform moving along the beam axis Z. Photoluminescence signal was transferred to the entrance of TRIAX Jobin-Yvon 190 spectrometer through an optical fiber. ANDOR iCCD was used to record luminescence spectra and MCP Hamamatsu R3809U-58 was used to record luminescence kinetics with a time resolution of ~50 ps.

The excitation density variation is achieved by moving the focusing lens along the laser beam, its 120 mm travel changes the size of the laser spot on the sample surface from 20 to 400 μ m in diameter. In the assumption of constant laser pulse output J, it allows for changing the excitation density by 400 times. The relation between the lens position Z and excitation fluence at the beam axis I_0 (in the maximum of Gaussian distribution) is given by the following equations [13]:

$$I_0(Z) = \frac{2}{\pi} \frac{J}{w(Z)^2} \quad (2)$$

$$w(Z) = w_0 \sqrt{1 + \left(\frac{M^2 \lambda Z}{\pi w_0^2} \right)^2}, w_0 = \sqrt{\frac{f \lambda}{\pi}} \quad (3)$$

Here, J is the energy of laser pulses (in our experiments J had the values of 1, 2, 5, 10, 20, 50, and 100 nJ), M^2 is the beam quality factor (for the third harmonic $M^2 \sim 1$), w_0 is the size of laser beam waist ($\sim 20 \mu\text{m}$), λ —exciting wavelength (266 nm), f —lens focusing distance.

3. Results

We shall start with the luminescence spectra of MAPbBr₃ measured with laser excitation to introduce some effects specific to hybrid perovskites. Figure 2 shows respective spectra measured at different temperatures and excitation densities. At relatively low excitation density ($I_0 = 7.6 \mu\text{J}/\text{cm}^2$), the luminescence spectra clearly exhibit an exciton feature, that is centered near the MAPbBr₃ absorption edge (Figure 2a). At 13 K the exciton peak is centered at 2.248 eV and has FWHM of approximately 18 meV. In addition, another peak is present, which is red-shifted compared to the exciton one by approximately 40 meV. This feature can be observed at ~ 40 K; however, its intensity gradually decreases with temperature and completely disappears by 80 K.

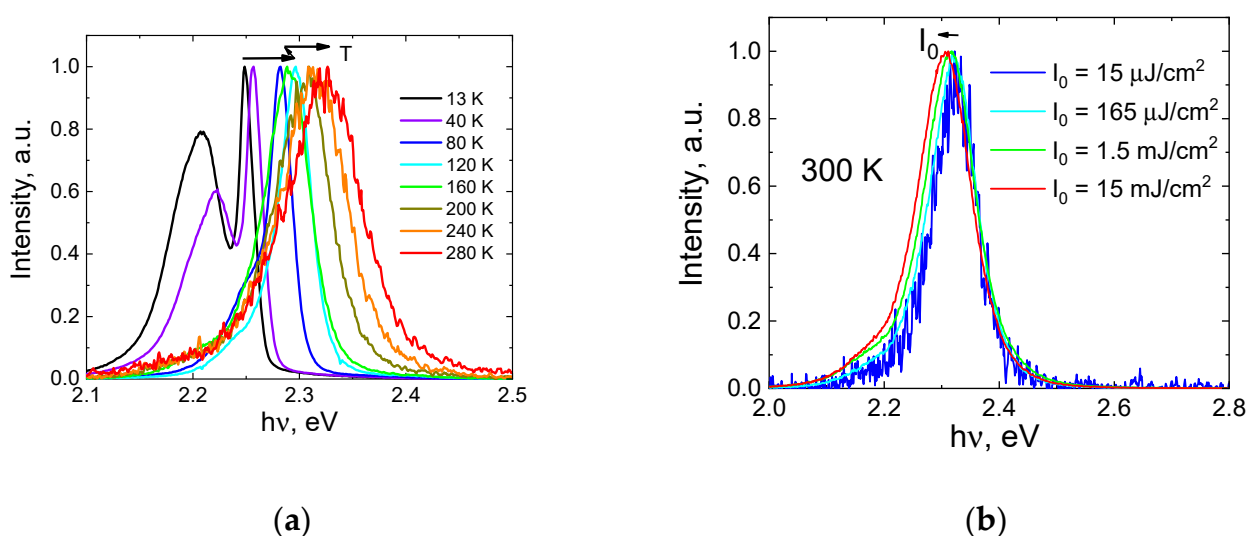


Figure 2. (a) Luminescence spectra of MAPbBr₃ excited with 4.65 eV laser pulses at different temperatures and fixed excitation density ($I_0 = 7.6 \mu\text{J}/\text{cm}^2$); (b) Luminescence spectra of MAPbBr₃ excited with 4.65 eV laser pulses at different excitation densities and fixed temperature (300 K). All presented spectra were divided by their maximum intensity. Arrows show the shift of the peak maximum position with the increase of temperature T (a) and excitation density I_0 (b).

The exciton peak shifts toward higher energies and slightly broadens with temperature. In the temperature range 140 K–160 K, we observe an abrupt change in the luminescence spectrum profile: luminescence maximum red-shifts by approximately 11 meV (from 2.3 to 2.289 eV) and the exciton peak widens by the factor of 1.67 (FWHM increases from 30 to 50 meV). This corresponds to the phase transition of MAPbBr₃ crystal lattice that changes its structure from the orthorhombic to tetragonal one at 145 K [16].

At temperatures above 160 K, only the exciton peak is left in the luminescence spectra. The second phase transition (from the tetragonal to cubic phase) is known to occur at 220 K [16]; however, it does not introduce substantial changes in the MAPbBr₃ luminescence spectrum. Exciton peak continues to gradually blue-shift and broaden with temperature until we finally arrive at room temperature, where the maximum position is 2.322 eV and FWHM is approximately 94 meV.

It should be noted that the position of the exciton luminescence peak is provided by different authors with substantial discrepancy, e.g., 2.175 eV in [14], 2.3 eV in [17], and 2.35 eV in [18]. Our experimental results allow us to somewhat account for this discrepancy, suggesting that the luminescence spectra profiles of MAPbBr₃ depend largely on excitation conditions. Figure 2b shows luminescence spectra measured at 300 K using the Z-scan technique. At higher excitation densities the maximum of luminescence spectra red-shifts

(from 2.334 eV at $I_0 = 1 \mu\text{J}/\text{cm}^2$ to 2.304 eV at $10 \text{ mJ}/\text{cm}^2$) and the exciton line broadens (from 94 meV at $I_0 = 1 \mu\text{J}/\text{cm}^2$ to 124 meV at $10 \text{ mJ}/\text{cm}^2$). A similar tendency was observed for other investigated temperatures. While this example does not cover all the variety of luminescence parameters reported in the literature, it clearly illustrates the influence of excitation conditions on the observed luminescence spectra. This issue is addressed further in the text.

For comparison, Figure 3a shows the luminescence spectrum measured with a different excitation source—a xenon lamp (80 K). Under these conditions, the exciton luminescence peak (marked as 1 in Figure 3a) is centered at 2.254 eV. However, with laser excitation at the same temperature, it is centered at 2.281 eV. The reason for that is in different penetration depths of 3 eV photons (xenon lamp excitation) and 4.65 eV photons (laser excitation), in the latter case, the absorption coefficient is several times higher. The effect of reabsorption of luminescence light increases with the penetration depth of the exciting radiation, strong reabsorption is due to small Stokes shift [19]. The value of the shift is illustrated by the luminescence excitation spectrum shown in the same graph.

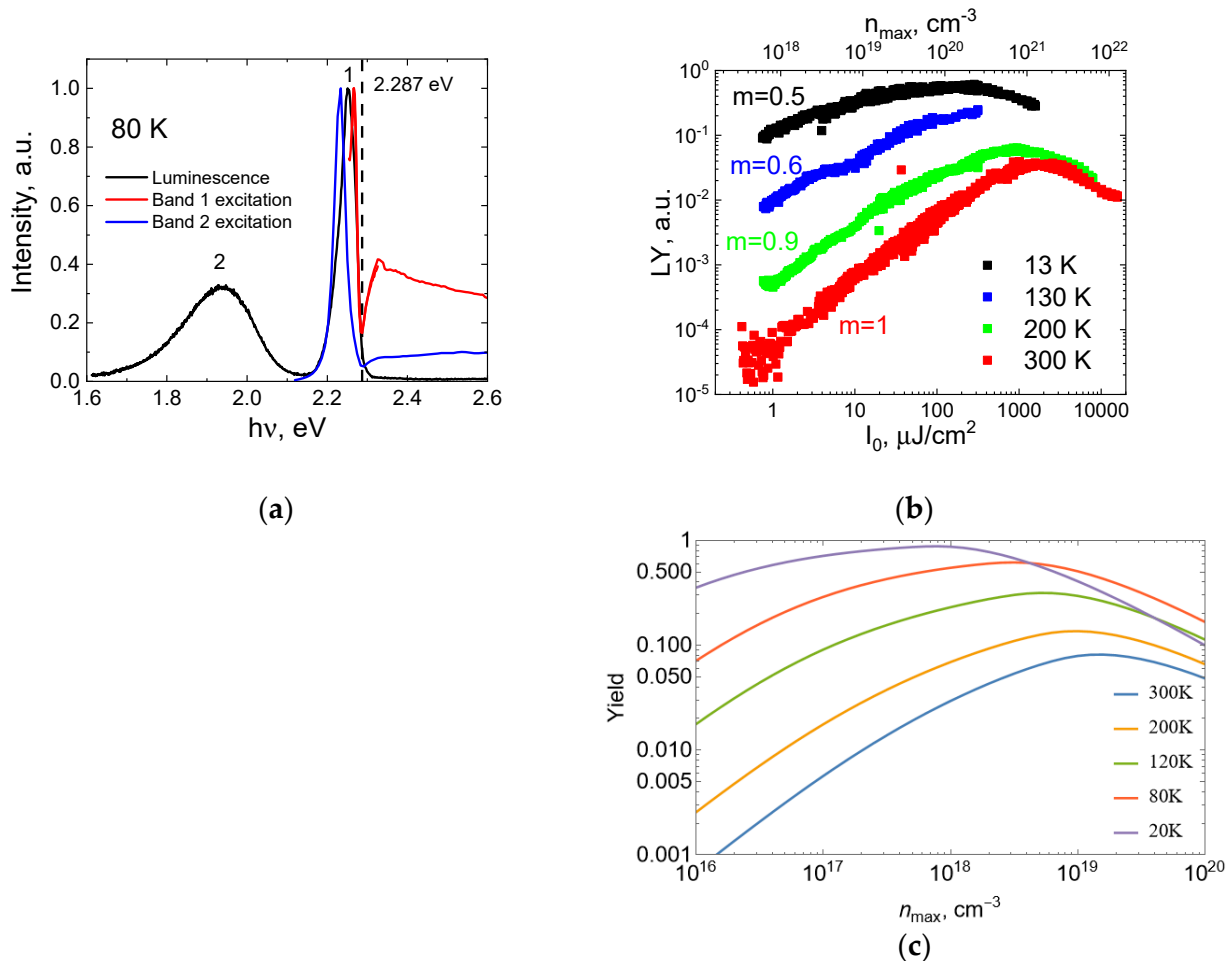


Figure 3. (a) Luminescence and luminescence excitation spectra of MAPbBr₃ excited with Xe-lamp at 80 K (for luminescence spectrum $h\nu_{\text{exc}} = 3 \text{ eV}$). All presented spectra were divided by their maximum intensity; (b) Excitation density dependence of relative light yield at different temperatures; m stands for the power index in the dependence $LY \sim (I_0)^m$; (c) simulation of panel (b) data using rate equations described in Appendix B.

Both the excitation spectrum of the excitonic luminescence and that of a defect emission (band 2 in Figure 3) have a local minimum at 2.287 eV. This minimum corresponds to the maximum of the absorption spectra manifested via surface losses. Quite often, the features

of the excitation spectra in the fundamental absorption region are anti-correlated with the features of the absorption, meaning that the minima of the excitation spectra coincide in position with the maxima of the absorption spectra and vice versa, which is usually explained by the surface losses (see [20–23] and Appendix A). So far, we did not find luminescence excitation spectra for MAPbBr₃ in the literature. In [24], such excitation spectrum for MAPbCl₃ was measured and it has quite a usual profile: the peak of the excitation spectrum coincides with that of the absorption. Diffusion of the charge carriers to the surface defects, where they recombine non-radiatively, is the origin of the observed effect. Renowned mobility of charge carriers in hybrid perovskites [25] supports this hypothesis and the strength of the effect in our case (though the sample was freshly cleaved prior to the measurements) indicates that the number of surface defects was large. An additional luminescence band peaking at 1.93 eV in the same figure can be attributed to defects in the bulk. It is efficiently excited in the region of exciton absorption; however, its highest yield is achieved at the low-energy tail of the exciton absorption, where the absorption coefficient is smaller and surface losses are less pronounced. To summarize, in our specific crystal, we must take into account losses due to the surface defects and defects in the bulk.

Figure 3b shows the dependence of luminescence light yield (LY) from the excitation density at different temperatures. By LY we mean the number of luminescence photons divided by the number of incident photons. There are two X-axes in the Figure, one with habitual $I_0 \mu\text{J}/\text{cm}^2$, and the other one, namely n_{max} , needs additional comments. The intensity of the laser light on the sample surface has a Gaussian distribution relative to the beam axis. The distribution of absorbed light into the sample depth obeys Beer's law. Thus, the distribution of carriers created by the light absorption will be strongly inhomogeneous both along the radial coordinate ρ and depth x . To characterize the density of created charge carriers we introduce n_{max} standing for the maximum concentration of carriers in the center of the laser spot near the surface:

$$n_{\text{max}}(Z) = \frac{2}{\pi} \frac{kI}{w(Z)^2 h\nu} = \frac{kI_0(Z)}{h\nu} \quad (4)$$

Here, $w(Z)$ and $I_0(Z)$ are described by formulae (2) and (3), k is the absorption coefficient of MAPbBr₃ taken for $h\nu = 4.65 \text{ eV}$ equal to $6 \times 10^5 \text{ cm}^{-1}$ [26]. The carrier distribution then will be written as:

$$n(\rho, x; Z) = n_{\text{max}}(Z) \exp\left(\frac{-2\rho^2}{w(Z)^2}\right) \exp(-kx) \quad (5)$$

Such effects as absorption saturation and charge carrier diffusion would affect this distribution resulting in the reduction of the actual maximum density. At RT the $LY(n_{\text{max}})$ or $LY(I_0)$ dependence can be subdivided into three areas: (i) an almost linear dependence of $LY(n_{\text{max}})$, which corresponds to a quadratic increase in the luminescence intensity with increasing photon density; (ii) for $n_{\text{max}} > 4 \times 10^{20} \text{ cm}^{-3}$ ($I_0 \sim 600 \mu\text{J}/\text{cm}^2$) slowing down of $LY(n_{\text{max}})$ growth with the saturation at $n_{\text{max}} \sim 10^{21} \text{ cm}^{-3}$; (iii) decrease in the $LY(n_{\text{max}})$ with further increase in the excitation density. These results are in good agreement with the works of [27]. Temperature dependence of the excitation density effects was not investigated previously. At room temperature, we see three orders of magnitude increase in the light yield with excitation density, while at 13 K it is less than one order. Moreover, the saturation of the yield is observed at different densities at different temperatures corresponding to the lowest one at 13 K.

It is natural to explain the observed effect by the conditions of the co-existence of excitons and electron–hole pairs changing with excitation density and temperature. The excitons decay radiatively and charge carriers can be trapped by defects. The ratio of the exciton concentration to the product of electrons and hole concentration in the stationary case depends on temperature and exciton binding energy and is described by kinetic equations in Appendix B. In our case of excitation by femtosecond laser pulses, we have to

account for the following dynamic processes: carrier capture by the defects, radiative decay of excitons, binding of electrons and holes into excitons, and a reverse process using rate equations. We also take account of the concentration-dependent exciton binding energy due to the screening effect [28], as well as the absence of excitonic states at concentrations above Mott density [29,30]. This approach gives qualitative agreement with experimental results (Figure 3c). The reproduced different density dependencies of luminescence yield at different temperatures, temperature-dependent positions of the maximum of respective curves, as well as the temperature-dependent slopes of the observed yield increase, cannot be attributed to a single process, a whole list of considered competing processes contributes to the observed features. The simulation gave the best agreement for exciton Rydberg energy of 40 meV.

The luminescence kinetics of MAPbBr₃ is also strongly affected by the excitation conditions as is demonstrated by Figure 4a with the temperature dependence of the kinetics. The instrument response function (IRF) is presented as well. All luminescence decay curves are strongly nonexponential: in the region of picosecond times, the kinetics is affected by the interaction of electronic excitations in the regions of their high density and/or competing channels such as precursor electron or hole capture by defects. In the nanosecond region, the origin of kinetics departure from the true radiative one is due to the processes of re-emission following re-absorption. The increase in the decay time depends on the number of reabsorption events, see, e.g., [31]. The region of larger times (not presented in the figure) is sensitive to electrons and holes released from shallow traps and binding into excitons (tens and hundreds of nanoseconds). To trace the trends in kinetics changing with temperature and excitation density they were parameterized using the following formula:

$$\tau = \int_0^{\infty} \frac{I_{lum}(t)}{I_{lum}(0)} dt = \frac{\int_0^{\infty} \sum_1^n \frac{A_i}{\tau_i} \exp(-t/\tau_i) dt}{\sum_1^n \frac{A_i}{\tau_i}} = \frac{\sum_1^n A_i}{\sum_1^n \frac{A_i}{\tau_i}}, \quad (6)$$

which allows the introduction of average decay time τ . An example of fitting parameters for decay kinetics at 200 K is shown in Table 1.

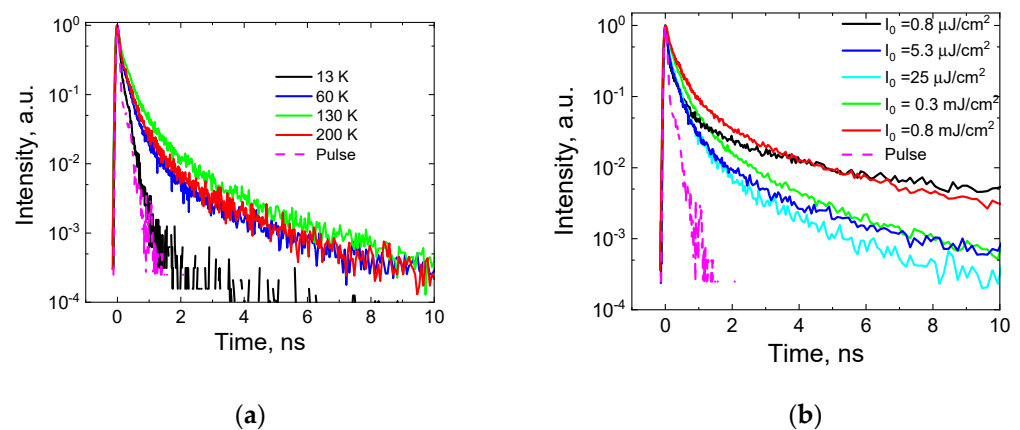


Figure 4. (a) Luminescence kinetics of MAPbBr₃ exciton peak excited with laser at different temperatures ($I_0 = 25 \mu\text{J}/\text{cm}^2$, $n_{\text{max}} = 1.7 \times 10^{19} \text{cm}^{-3}$); (b) Luminescence kinetics of MAPbBr₃ exciton peak excited with laser at different excitation densities ($T = 200 \text{K}$).

At 13 K, the decay is very close to IRF, the average decay time can be evaluated as ~ 55 ps. This value is substantially smaller than the nanoseconds presented, e.g., in [32]. The difference is due to quenching by defects in agreement with concentrations used in Appendix B for simulation. With temperature increases up to 130 K, the decays slow down, and the average decay constant is ~ 120 ps. Further increase in the temperature results in the opposite effect: at 200 K decay is faster, than at 130 K with an average time of ~ 100 ps. This effect can be attributed to the phase transition.

Table 1. Fitting parameters for MAPbBr₃ decay kinetics at 200 K.

I_0 , $\mu\text{J}/\text{cm}^2$	τ_1 , ps (A_1)	τ_2 , ns (A_2)	τ_3 , ns (A_3)	τ , ps
0.8	40 (0.38)	0.45 (0.22)	5 (0.4)	100
5.3	50 (0.47)	0.32 (0.38)	2.5 (0.15)	94
25	50 (0.47)	0.3 (0.38)	1.5 (0.15)	93
300	80 (0.41)	0.4 (0.41)	2.3 (0.18)	161
800	80 (0.28)	0.5 (0.42)	3.5 (0.3)	226

It should be noted that luminescence kinetics observed with laser excitation at temperatures above 60 K agree rather well both with our measurements under X-ray excitation and with literature data [32]; however, at 13 K, our decay is much faster than measured in [32]. The reason for that is discussed in the next section. Figure 4b shows the kinetics of exciton luminescence at different excitation densities (at 200 K). In the range of I_0 from 0.8 to 25 $\mu\text{J}/\text{cm}^2$ ($n_{\text{max}} \sim 5 \times 10^{17} - 2 \times 10^{19} \text{ cm}^{-3}$), the subnanosecond part of decay kinetics with $\tau < 1$ ns remains the same, on the contrary, the slower nanosecond component decreases and this tendency is confirmed by the decrease in the average decay time to 93 ps. With a further increase in $I_0 \sim 25 - 800 \mu\text{J}/\text{cm}^2$, both picosecond and nanosecond decay components slow down and the average time increases from 100 to 220 ps.

4. Discussion

In the previous section, we have shown that the luminescence spectra profile depends on the excitation conditions. It is important to note that most changes occur in the higher-energy part of the spectra, while the lower-energy wing of the luminescence band stays almost unchanged. This is illustrated by Figure 5a, where luminescence spectra measured at different excitation conditions (laser excitation with different excitation density, Xe-lamp excitation, X-ray excitation) are normalized to the low-energy wing (at an arbitrary temperature of 130 K).

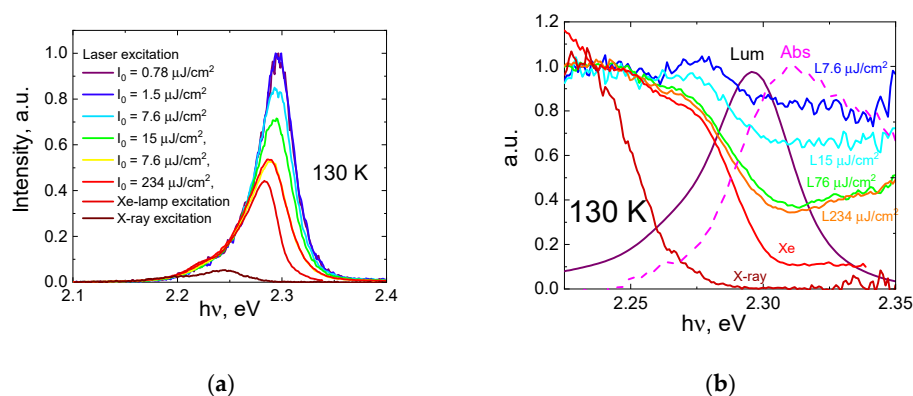


Figure 5. (a) Luminescence spectra of MAPbBr₃ in different excitation conditions (130 K). The spectra are normalized to the low-energy wing of the luminescence spectra; (b) Result of dividing the luminescence spectra measured at different excitation densities (values for I_0 are marked at graph, e.g., $L7.6\mu\text{J}/\text{cm}^2$ means laser excitation with $I_0 = 7.6 \mu\text{J}/\text{cm}^2$) and normalized to their long wavelength side by the spectrum measured at the lowest density ($I_0 = 0.78 \mu\text{J}/\text{cm}^2$), that is represented on the graph by purple line marked as Lum. The estimated absorption spectrum is shown on the graph by dashed magenta line and is marked as Abs.

One of the effects modulating the profile of the emission spectra depending on the excitation density, energy, and temperature is the re-absorption, which in hybrid perovskites is known to be quite pronounced. It is problematic to measure absorption in this spectral range from a single crystal in a wide dynamic range from the Urbach tail (10^2 cm^{-1}) to the excitonic absorption (10^5 cm^{-1}). Absorption spectra found in the literature are quite different and depend on many factors such as the quality of the samples, surface conditions, method of the measurements, etc. [18,26,33–35]. The depth of luminescence escape, defined in a simple case by Beer's law only (neglecting surface losses and diffusion, which accounts for the actual charge carrier distribution) can be described as:

$$I \sim S(h\nu) \exp(-k_{em}(h\nu)\langle x_{em} \rangle) \quad (7)$$

where $S(h\nu)$ is the true profile of the luminescence spectrum (in the bulk), $k_{em}(h\nu)$ is the absorption coefficient, and $\langle x_{em} \rangle$ is an averaged coordinate of the emitting exciton. Assuming that, for various excitation conditions, we can introduce respective $\langle x_{em} \rangle$, dividing two luminescence spectra differently according to the excitation energy or excitation density yields $\exp(-k_{em}(h\nu)\langle x_{em1} \rangle) / \exp(-k_{em}(h\nu)\langle x_{em2} \rangle)$, which can be re-written as $\exp(-k_{em}(h\nu)(\langle x_{em1} \rangle - \langle x_{em2} \rangle))$. Thus we tried to evaluate the re-absorption by dividing the luminescence spectra measured at different excitation densities and normalized to their long wavelength side by the spectrum measured at the lowest density (the resulting curves are shown in Figure 5b). The absorption spectrum multiplied by an unknown constant $\langle x_{em1} \rangle - \langle x_{em2} \rangle$ is shown by a magenta dashed line in Figure 5b. It represents a spectral distribution of normalized absorption, its absolute value can be obtained from the comparison with experimental values from the literature, e.g., measured by ellipsometry [26]. Now, we can estimate the dependence of the shift $\langle x_{em1} \rangle - \langle x_{em2} \rangle$ of the emitting point on the measurement conditions. As a denominator, we used the luminescence spectrum measured at a low density of $0.78 \mu\text{J}/\text{cm}^2$ laser radiation at 4.65 eV with the shortest penetration depth of $\sim 17 \text{ nm}$ [26] least affected by the re-absorption. The excitation density of $15 \mu\text{J}/\text{cm}^2$ results in the shift of the emitting point by 65 nm, for $230 \mu\text{J}/\text{cm}^2$ this value is 140 nm. An increase in $\langle x_{em1} \rangle$ value with the excitation density is related to the absorption saturation. Excitation with a xenon lamp at 3 eV gives about a 300 nm increase in the escape depth while the penetration depth for 3 eV photons is 150 nm. This discrepancy is well explained by the diffusion of the charge carriers. The difference $300 \text{ nm} - 150 \text{ nm} = 150 \text{ nm}$ can be used for the evaluation of the diffusion length for our specific crystal. This value falls within the range provided in the literature but from its low side, it is much less than the tens of microns suggested in [36]. The important role of defects in our crystals (defining short diffusion length) is confirmed by decay kinetics of the excitons with a very short characteristic decay time of the order of tens of picoseconds even at low temperature ($L = \sqrt{D\tau}$). X-ray excitation (19 keV) penetrates to a depth of $\sim 100 \mu\text{m}$, hence luminescence light has to travel a long distance before the escape and the observer sees only a part of the spectrum corresponding to the region, where the absorption is low. More accurately, re-absorption is considered in Appendix A.

Re-absorption inherent to the studied perovskite limits its application as a scintillator for spectrometer measurements and in cases that require high energy resolution. However, its fast decay, which can be controlled by material engineering, can be quite attractive for applications demanding high coincidence time resolution.

5. Conclusions

The luminescent Z-scan technique with time resolution applied to hybrid perovskite crystals of $\text{CH}_3\text{NH}_3\text{PbBr}_3$ was used to establish the hierarchy of relaxation processes in this material. The influence of absorption saturation, charge carrier diffusion, and luminescence reabsorption effects are discussed. Modification of the emission spectra profiles with the excitation density was demonstrated to be related to the changes in the depth of the excited region, and evaluation of the carrier diffusion length was performed. The presented approach can explain the discrepancy in the position of exciton emission peak and exciton

decay characteristics found in the literature. Dependence of the light yield on the excitation density at different temperatures was simulated using kinetic equations describing electron (hole) and exciton concentrations with the account for electron (hole) capture by defects, binding of electrons and holes into excitons and a reverse process of exciton decomposition. The binding energy of the exciton was taken as a function of electron concentration (screening and Mott transition). Experimentally observed changes in the slope of the light yield increase with the excitation density are reproduced well using Rydberg exciton binding energy of 40 meV. The unusual coexistence of high charge carrier mobility and reasonable yield of excitonic luminescence that make hybrid perovskites attractive both for photovoltaics and scintillator applications (extremely exceptional) is explained by the presented results: at low excitation densities at RT mainly separated e-h pairs are created with the probability of binding into exciton increasing with excitation density. As was discussed in the introduction, in scintillators, ionizing radiation creates clusters with a high density of excitations, and these clusters will act as “luminescent centers” in this context. The suggested scintillation mechanism makes hybrid perovskite materials inappropriate for applications requiring energy resolution; however, the fast decay time of their excitonic emission with a characteristic decay time of several nanoseconds, which can be reduced to several tens of picoseconds, makes them attractive for fast-timing applications.

Author Contributions: Conceptualization, A.N.V. and A.N.B.; methodology, N.A.F. and P.M.; software, A.N.V. and E.D.R.; validation, I.N.S., D.A.S.; formal analysis, E.D.R. and I.A.F.; investigation, N.A.F., A.N.B. and P.M.; resources, B.I.Z. and P.M.; data curation, E.D.R.; writing—original draft preparation, E.D.R.; writing—review and editing, I.A.K.; visualization, E.D.R. All authors have read and agreed to the published version of the manuscript.

Funding: This research received no external funding.

Data Availability Statement: Data sharing not applicable.

Acknowledgments: This work is supported in part by the Ministry of Science and Higher Education of the Russian Federation, grant No. 075-15-2021-1353. The European Union’s Horizon 2020 research and innovation programme under grant agreement no. CNRS-CELIA002677 Laserlab-Europe is acknowledged.

Conflicts of Interest: The authors declare no conflict of interest.

Appendix A. Account for reabsorption in case of diffusion of excitations

In simplified approximation, the reabsorption of exciton emission does not result in re-emission (if the emission yield is low), and we can estimate the decrease in the emission produced at a distance x from the surface $e^{-k_{em}(hv)x}$ (if the observation is in the direction normal to the surface). In the case of the exciton diffusion, we can obtain the evolution of exciton concentration from a simple diffusion coefficient with initial condition

$$n_{ex}(x, 0) = n_0 k_{ex} e^{-k_{ex}x}. \quad (A1)$$

Here, k_{ex} and $k_{em}(hv)$ are the absorption coefficients for exciting photons and photons of luminescence. The diffusion equation can be solved in different boundary conditions. In the case of strong surface quenching, $n_{ex}(x, t)|_{x=0} = 0$; whereas in the case without surface quenching, the flux of the carriers through the surface equals zero: $\partial n_{ex}(x, t)/\partial x|_{x=0} = 0$.

The resulting yield of the emission in the case of strong surface quenching is equal to

$$Y_{SQ} = \frac{k_{ex}}{(k_{ex} + k_{em}(hv))(1 + k_{ex}L)(1 + k_{em}(hv)L)}, \quad (A2)$$

whereas for the case w/o quenching

$$Y_{w/oSQ} = \frac{k_{ex}(1 + k_{ex}L + k_{em}(hv)L)}{(k_{ex} + k_{em}(hv))(1 + k_{ex}L)(1 + k_{em}(hv)L)}. \quad (A3)$$

Here, $L = \sqrt{D\tau_{em}}$ is the diffusion length of the excitations with diffusion coefficient D during the emission time τ_{em} . Formula (A2) in case of neglecting the re-absorption describes the excitation spectrum presented in Figure 3a:

$$Y_{SQ} = \frac{1}{1 + k_{ex}L}, \quad k_{em}(h\nu) \ll k_{ex} \text{ or } 1/L, \quad (\text{A4})$$

resulting in a dip in the exciton energy in this spectrum. In the case of neglecting diffusion ($L = 0$), formula (A3) corresponds to the expression $\frac{k_{ex}}{k_{ex} + k_{em}(h\nu)}$ used in [24].

For relatively small reabsorption ($k_{em}(h\nu) \leq k_{ex}$ or $1/L$), we can use approximate formulas instead of (A2) and (A3):

$$Y_{SQ} = \frac{1}{1 + k_{ex}L} \left(1 - (k_{ex}^{-1} + L)k_{em}(h\nu) \right) \approx \frac{1}{1 + k_{ex}L} \exp\left(- (k_{ex}^{-1} + L)k_{em}(h\nu)\right). \quad (\text{A5})$$

and

$$Y_{w/oSQ} \approx \exp\left(- \frac{k_{ex}^{-2} + k_{ex}^{-1}L + L^2}{k_{ex}^{-1} + L} k_{em}(h\nu)\right). \quad (\text{A6})$$

Such exponential approximations for the correction of emission spectra were used in the analysis of Figure 5b.

Appendix B. Rate equations for simulation of the evolution of excited region

The evolution of excited region containing electrons with time and spatial dependence of concentration $n_e(x, t)$, holes ($n_h(x, t)$), and excitons ($n_{ex}(x, t)$) can be described using the following set of equations:

$$\begin{aligned} \frac{\partial n_e(x, t)}{\partial t} &= D_e \frac{\partial^2 n_e(x, t)}{\partial x^2} - \beta n_e^2(x, t) + \gamma n_{ex}(x, t) - p n_e(x, t), \\ \frac{\partial n_{ex}(x, t)}{\partial t} &= D_{ex} \frac{\partial^2 n_{ex}(x, t)}{\partial x^2} - \tau_{ex}^{-1} n_{ex}(x, t) + \beta n_e^2(x, t) - \gamma n_{ex}(x, t). \end{aligned} \quad (\text{A7})$$

Here, we assume that the concentration of holes equals that of electrons and no effects of ambipolar diffusion due to different electron and hole diffusion coefficients $D_e = D_h$ are observed. Therefore, we can assume that $n_e(x, t) = n_h(x, t)$ for simplification. This assumption can be justified since the effective masses and mobilities of electrons and holes do not differ significantly in this material. We assume that electrons and holes can be captured by bulk defects at the rate p (which is about 10 to 100 ns⁻¹), and excitons can emit photons with radiation time τ_{ex} (about 1 ns). The term $\beta n_e^2(x, t) \equiv \beta n_e(x, t)n_h(x, t)$ describes the bi-molecular binding of electron and hole into exciton, term $\gamma n_{ex}(x, t)$ corresponds to the reverse reaction, i.e., decomposition of exciton into e-h pair. The ratio between β and γ can be estimated using thermodynamics consideration. Simply, with the assumption that all processes except the discussed binding and decomposition can be neglected, the concentrations are in thermodynamic equilibrium $\beta n_e^2 = \gamma n_{ex}$. In this case, the concentrations should obey the Saha equation [37] and we can take

$$\frac{\gamma}{\beta} = \left(\frac{\mu k_B T}{2\pi \hbar^2} \right)^{3/2} e^{-\frac{E_b}{k_B T}}. \quad (\text{A8})$$

Here, μ is the effective mass of the carriers (all masses are about the same). Definitely, the time-dependent concentrations in real cases do not correspond to the Saha relation due to other terms in equations (A7), but we believe we can keep it for the ratio of gamma and beta. We assume that exciton binding energy E_b changes with electron density due to the screening effect as

$$E_b = E_{b0} \left(1 - 2 \left(\frac{n_e}{n_M} \right)^{1/2} + \frac{3}{2} \frac{n_e}{n_M} \right), \quad (\text{A9})$$

where E_{b0} is the Rydberg exciton, and n_M is the Mott density at which excitons disappear. In Debye–Hückel approximation [28]

$$n_M = 0.71 \frac{k_B T}{a_B^3 E_{b0}}. \quad (\text{A10})$$

We do not include one term in the set (A7), which is especially important in the case of low-intensity excitation, namely the geminate (genetic) binding term of the correlated electrons and holes into excitons. This term is linear with respect to electron concentration and describes the recombination of an electron and a hole created by the same photon. Bi-molecular (stochastic) recombination dominates if the distance between events of photon absorption is less than the thermalization length of electrons and holes created with total kinetic energy $h\nu - E_g$. The femtosecond laser excitation is powerful enough to meet this criterion.

If we neglect diffusion, the system (A7) becomes a simple ODE system, which can be solved at each point x for the initial condition at any radial point ρ

$$n_e(x, 0; \rho) = n_{\max} e^{-2\rho^2/w(z)^2} k e^{-kx}. \quad (\text{A11})$$

The resulting emission yield from any point with initial electron concentration n_0 can be calculated as

$$Y(n_0) = \tau_{ex}^{-1} \int_0^{\infty} n(t) dt. \quad (\text{A12})$$

This result should be averaged over the Gaussian distribution of the initial concentration n_0 in the surface plain and exponential distribution over the depth. This averaging can be performed using the weight function [38]:

$$\bar{Y}(n_{\max}) = \int_0^{n_{\max}} Y(n) \frac{1}{n} \ln\left(\frac{n_{\max}}{n}\right) dn. \quad (\text{A13})$$

The qualitative results obtained from the solution of these equations for $E_{b0} = 40$ meV are presented in Figure 3c in the main text.

References

1. Korzhik, M.; Tamulaitis, G.; Vasil'ev, A.N. *Physics of Fast Processes in Scintillators*; Particle Acceleration and Detection; Springer International Publishing: Cham, Switzerland, 2020; ISBN 978-3-030-21965-9.
2. Belsky, A.; Lebbou, K.; Kononets, V.; Sidletskiy, O.; Gektin, A.; Auffray, E.; Spassky, D.; Vasil'ev, A.N. Mechanisms of Luminescence Decay in YAG-Ce,Mg Fibers Excited by γ - and X-rays. *Opt. Mater.* **2019**, *92*, 341–346. [CrossRef]
3. Gektin, A.; Vasil'ev, A. Scintillator Energy Resolution and a Way to Improve It by Kinetic Waveform Analysis. *Radiat. Meas.* **2019**, *122*, 108–114. [CrossRef]
4. Gektin, A.V.; Vasil'ev, A.N. Fluctuations of Ionizing Particle Track Structure and Energy Resolution of Scintillators. *Funct. Mater.* **2017**, *4*, 621–627. [CrossRef]
5. Itoh, N.; Stoneham, A.M. Materials Modification by Electronic Excitation. *Radiat. Eff. Defects Solids* **2001**, *155*, 277–290. [CrossRef]
6. Lecoq, P. Pushing the Limits in Time-of-Flight PET Imaging. *IEEE Trans. Radiat. Plasma Med. Sci.* **2017**, *1*, 473–485. [CrossRef]
7. Lecoq, P.; Korzhik, M.; Vasiliev, A. Can Transient Phenomena Help Improving Time Resolution in Scintillators? *IEEE Trans. Nucl. Sci.* **2014**, *61*, 229–234. [CrossRef]
8. Grim, J.Q.; Ucer, K.B.; Burger, A.; Bhattacharya, P.; Tupitsyn, E.; Rowe, E.; Buliga, V.M.; Trefilova, L.; Gektin, A.; Bizarri, G.A.; et al. Nonlinear Quenching of Densely Excited States in Wide-Gap Solids. *Phys. Rev. B* **2013**, *87*, 125117. [CrossRef]
9. Kirm, M.; Nagirnyi, V.; Feldbach, E.; De Grazia, M.; Carré, B.; Merdji, H.; Guizard, S.; Geoffroy, G.; Gaudin, J.; Fedorov, N.; et al. Exciton-Exciton Interactions in CdWO₄ Irradiated by Intense Femtosecond Vacuum Ultraviolet Pulses. *Phys. Rev. B* **2009**, *79*, 233103. [CrossRef]
10. Spassky, D.; Vasil'ev, A.; Krutyak, N.; Buzanov, O.; Morozov, V.; Belik, A.; Fedorov, N.; Martin, P.; Belsky, A. Decay Kinetics of Gd₃Al₂Ga₃O₁₂:Ce³⁺ Luminescence under Dense Laser Irradiation. *Materials* **2023**, *16*, 971. [CrossRef]

11. Spassky, D.; Vasil'ev, A.; Belsky, A.; Fedorov, N.; Martin, P.; Markov, S.; Buzanov, O.; Kozlova, N.; Shlegel, V. Excitation Density Effects in Luminescence Properties of CaMoO_4 and ZnMoO_4 . *Opt. Mater.* **2019**, *90*, 7–13. [[CrossRef](#)]
12. Nagirnyi, V.; Dolgov, S.; Grigonis, R.; Kirm, M.; Nagornaya, L.L.; Savikhin, F.; Sirutkaitis, V.; Vielhauer, S.; Vasil'ev, A. Exciton–Exciton Interaction in CdWO_4 Under Resonant Excitation by Intense Femtosecond Laser Pulses. *IEEE Trans. Nucl. Sci.* **2010**, *57*, 1182–1186. [[CrossRef](#)]
13. Belsky, A.; Fedorov, N.; Gridin, S.; Gektin, A.; Martin, P.; Spassky, D.; Vasil'ev, A. Time-Resolved Luminescence Z-Scan of CsI Using Power Femtosecond Laser Pulses. *Radiat. Meas.* **2019**, *124*, 1–8. [[CrossRef](#)]
14. Shi, D.; Adinolfi, V.; Comin, R.; Yuan, M.; Alarousu, E.; Buin, A.; Chen, Y.; Hoogland, S.; Rothenberger, A.; Katsiev, K.; et al. Low Trap-State Density and Long Carrier Diffusion in Organolead Trihalide Perovskite Single Crystals. *Science* **2015**, *347*, 519–522. [[CrossRef](#)]
15. Fedorov, N.; Beaulieu, S.; Belsky, A.; Blanchet, V.; Bouillaud, R.; De Anda Villa, M.; Filippov, A.; Fourment, C.; Gaudin, J.; Grisenti, R.E.; et al. Aurore: A Platform for Ultrafast Sciences. *Rev. Sci. Instrum.* **2020**, *91*, 105104. [[CrossRef](#)]
16. Wang, K.-H.; Li, L.-C.; Shellaiah, M.; Wen Sun, K. Structural and Photophysical Properties of Methylammonium Lead Tribromide (MAPbBr_3) Single Crystals. *Sci. Rep.* **2017**, *7*, 13643. [[CrossRef](#)]
17. Kunugita, H.; Hashimoto, T.; Kiyota, Y.; Udagawa, Y.; Takeoka, Y.; Nakamura, Y.; Sano, J.; Matsushita, T.; Kondo, T.; Miyasaka, T.; et al. Excitonic Feature in Hybrid Perovskite $\text{CH}_3\text{NH}_3\text{PbBr}_3$ Single Crystals. *Chem. Lett.* **2015**, *44*, 852–854. [[CrossRef](#)]
18. Kitazawa, N.; Watanabe, Y.; Nakamura, Y. Optical Properties of $\text{CH}_3\text{NH}_3\text{PbX}_3$ (X = Halogen) and Their Mixed-Halide Crystals. *J. Mater. Sci.* **2002**, *37*, 3585–3587. [[CrossRef](#)]
19. Tilchin, J.; Dirin, D.N.; Maikov, G.I.; Sashchiuk, A.; Kovalenko, M.V.; Lifshitz, E. Hydrogen-like Wannier–Mott Excitons in Single Crystal of Methylammonium Lead Bromide Perovskite. *ACS Nano* **2016**, *10*, 6363–6371. [[CrossRef](#)]
20. Ackermann, C.; Brodmann, R.; Hann, U.; Suzuki, A.; Zimmerer, G. Photoluminescence Excitation Spectra of Solid Krypton. *Phys. Status Solidi B* **1976**, *74*, 579–590. [[CrossRef](#)]
21. Belsky, A.N.; Krupa, J.C. Luminescence Excitation Mechanisms of Rare Earth Doped Phosphors in the VUV Range. *Displays* **1999**, *19*, 185–196. [[CrossRef](#)]
22. Belskiy, A.N.; Kamenskikh, I.A.; Mikhailin, V.V.; Shpinkov, I.N.; Vasil'ev, A.N. Electronic Excitations in Crystals with Complex Oxyanions. *Phys. Scr.* **1990**, *41*, 530–536. [[CrossRef](#)]
23. Abrams, B.L.; Holloway, P.H. Role of the Surface in Luminescent Processes. *Chem. Rev.* **2004**, *104*, 5783–5802. [[CrossRef](#)] [[PubMed](#)]
24. Yamada, T.; Aharen, T.; Kanemitsu, Y. Near-Band-Edge Optical Responses of $\text{CH}_3\text{NH}_3\text{PbCl}_3$ Single Crystals: Photon Recycling of Excitonic Luminescence. *Phys. Rev. Lett.* **2018**, *120*, 057404. [[CrossRef](#)] [[PubMed](#)]
25. Milot, R.L.; Eperon, G.E.; Snaith, H.J.; Johnston, M.B.; Herz, L.M. Temperature-Dependent Charge-Carrier Dynamics in $\text{CH}_3\text{NH}_3\text{PbI}_3$ Perovskite Thin Films. *Adv. Funct. Mater.* **2015**, *25*, 6218–6227. [[CrossRef](#)]
26. Leguy, A.M.; Azarhoosh, P.; Alonso, M.I.; Campoy-Quiles, M.; Weber, O.J.; Yao, J.; Bryant, D.; Weller, M.T.; Nelson, J.; Walsh, A.; et al. Experimental and Theoretical Optical Properties of Methylammonium Lead Halide Perovskites. *Nanoscale* **2016**, *8*, 6317–6327. [[CrossRef](#)]
27. Sarritzu, V.; Sestu, N.; Marongiu, D.; Chang, X.; Wang, Q.; Loi, M.A.; Quochi, F.; Saba, M.; Mura, A.; Bongiovanni, G. Perovskite Excitons: Primary Exciton Creation and Crossover from Free Carriers to a Secondary Exciton Phase. *Adv. Opt. Mater.* **2018**, *6*, 1700839. [[CrossRef](#)]
28. Klingshirn, C.F. *Semiconductor Optics*; Graduate Texts in Physics; Springer: Berlin/Heidelberg, Germany, 2012; ISBN 978-3-642-28361-1.
29. Zimmermann, R.; Stolz, H. The Mass Action Law in Two-Component Fermi Systems Revisited Excitons and Electron-Hole Pairs. *Phys. Status Solidi B* **1985**, *131*, 151–164. [[CrossRef](#)]
30. Stolz, H.; Zimmermann, R. Correlated Pairs and a Mass Action Law in Two-Component Fermi Systems Excitons in an Electron-Hole Plasma. *Phys. Status Solidi B* **1979**, *94*, 135–146. [[CrossRef](#)]
31. Cheng, Z.; O'Carroll, D.M. Photon Recycling in Semiconductor Thin Films and Devices. *Adv. Sci.* **2021**, *8*, 2004076. [[CrossRef](#)]
32. Mykhaylyk, V.B.; Kraus, H.; Saliba, M. Bright and Fast Scintillation of Organolead Perovskite MAPbBr_3 at Low Temperatures. *Mater. Horiz.* **2019**, *6*, 1740–1747. [[CrossRef](#)]
33. Soufiani, A.M.; Huang, F.; Reece, P.; Sheng, R.; Ho-Baillie, A.; Green, M.A. Polaronic Exciton Binding Energy in Iodide and Bromide Organic-Inorganic Lead Halide Perovskites. *Appl. Phys. Lett.* **2015**, *107*, 231902. [[CrossRef](#)]
34. Tanaka, K.; Takahashi, T.; Ban, T.; Kondo, T.; Uchida, K.; Miura, N. Comparative Study on the Excitons in Lead-Halide-Based Perovskite-Type Crystals $\text{CH}_3\text{NH}_3\text{PbBr}_3$ $\text{CH}_3\text{NH}_3\text{PbI}_3$. *Solid State Commun.* **2003**, *127*, 619–623. [[CrossRef](#)]
35. Mannino, G.; Deretzi, I.; Smecca, E.; La Magna, A.; Alberti, A.; Ceratti, D.; Cahen, D. Temperature-Dependent Optical Band Gap in CsPbBr_3 , MAPbBr_3 , and FAPbBr_3 Single Crystals. *J. Phys. Chem. Lett.* **2020**, *11*, 2490–2496. [[CrossRef](#)]
36. McClintock, L.; Xiao, R.; Hou, Y.; Gibson, C.; Travaglini, H.C.; Abramovitch, D.; Tan, L.Z.; Senger, R.T.; Fu, Y.; Jin, S.; et al. Temperature and Gate Dependence of Carrier Diffusion in Single Crystal Methylammonium Lead Iodide Perovskite Microstructures. *J. Phys. Chem. Lett.* **2020**, *11*, 1000–1006. [[CrossRef](#)]

37. Saba, M.; Quochi, F.; Mura, A.; Bongiovanni, G. Excited State Properties of Hybrid Perovskites. *Acc. Chem. Res.* **2016**, *49*, 166–173. [[CrossRef](#)]
38. Vasil'ev, A.N. From Luminescence Non-Linearity to Scintillation Non-Proportionality. *IEEE Trans. Nucl. Sci.* **2008**, *55*, 1054–1061. [[CrossRef](#)]

Disclaimer/Publisher's Note: The statements, opinions and data contained in all publications are solely those of the individual author(s) and contributor(s) and not of MDPI and/or the editor(s). MDPI and/or the editor(s) disclaim responsibility for any injury to people or property resulting from any ideas, methods, instructions or products referred to in the content.